JOURNAL OF AIRCRAFT
Vol. 37, No. 1, January–February 2000

# Role of Stall Flutter in the Double-Stall Phenomenon of Wind-Turbine Blades

Lars E. Ericsson*
*Mountain View, California 94040*

**A study of existing experimental and computational results for the sectional aerodynamic characteristics of blades on wind turbines operating at full power shows that stall flutter, i.e., the blade bending response to the separated flow environment, plays a decisive role in the observed double-stall phenomenon.**

## Nomenclature

$C_{m\theta}$ = $\partial C_m/\partial\theta$
$C_{m\dot\theta}$ = $\partial C_m/\partial(\dot\theta c/U_\infty)$
$c$ = blade section chord
$f$ = oscillation frequency
$K_1$, $K_2$ = proportionality constants, Eqs. (2) and (4), respectively
$L$ = lift coefficient, $C_L = L/(\rho_\infty U_\infty^2/2)S$
$L'$ = sectional lift coefficient, $c_l = L'/(\rho_\infty U_\infty^2/2)c$
$M'$ = sectional pitching moment coefficient, $c_m = M'/(\rho_\infty U_\infty^2/2)c^2$
$N$ = normal force coefficient, $C_N = N/(\rho_\infty U_\infty^2/2)S$
$N'$ = sectional normal force coefficient, $c_n = N'/(\rho_\infty U_\infty^2/2)c$
$p$ = static pressure coefficient, $C_p = (p - p_\infty)/(\rho_\infty U_\infty^2/2)$
$R$ = rotor radius
$Re$ = Reynolds number based on $c$ and freestream conditions
$r_N$ = airfoil nose radius (Fig. 9)
$S$ = reference area
$t$ = time
$U$ = horizontal velocity
$U_w$ = wall velocity
$V$ = resultant velocity
$x$ = axial body-fixed coordinate
$y$ = spanwise coordinate
$z$ = space-fixed vertical coordinate, positive downward
$\alpha$ = angle of attack
$\dot\alpha$ = $\partial\alpha/\partial t$
$\bar\alpha$ = effective angular amplitude, Eq. (3)
$\alpha_{\text{eff}}$ = effective angle of attack, Eq. (3)
$\Delta$ = increment or amplitude
$\Delta\zeta$ = dimensionless amplitude, $\Delta z/c$
$\eta$ = dimensionless $y$ coordinate, $y/R$
$\theta$ = angular pitch perturbation
$\theta^*$ = effective angular pitch perturbation, Eq. (3)
$\xi$ = dimensionless $x$ coordinate, $x/c$
$\rho$ = air density
$\Omega$ = dimensionless flat-spin rate, $\omega R/U_\infty$
$\omega$ = angular frequency, $2\pi f$
$\bar\omega$ = reduced frequency, $\omega c/U_\infty$

*Subscripts*

crit = critical
$e$ = edge of boundary layer
max = maximum
$N$ = nose
$o$ = mean, time-average value
$s$ = separation
$W$ = wall
1, 2 = numbering subscript
$\infty$ = freestream conditions

Received 6 February 1999; revision received 20 July 1999; accepted for publication 28 July 1999. 

*Engineering Consultant. Fellow AIAA.

## Introduction

THE unique role played by the dynamic-stall phenomenon in the operation of wind turbines was recently described by Rasmussen et al.[1] Wind-turbine blades operate continuously under stalled flow conditions with relatively small variations of the angle of attack. This is in sharp contrast to a helicopter rotor, for which much of the early dynamic-stall research was performed, where the blade section operates over a large cyclic angle-of-attack range including both attached and separated flow conditions.[2] Although dynamic-stall measurements under the steadily stalled flow conditions typical for the blade section of a wind turbine have also been performed in support of stall flutter analyses,[3] not until now has the available database been used to describe the flow physics of the double-stall phenomenon.

## Background

The phenomenon of double stall is unique to the operating environment of wind turbines[4] (Fig. 1). In a certain wind speed range 15 m/s < $U_\infty$ < 18 m/s, the power output dropped roughly 150 kW for a period of about one hour, after which the power regained its normal value. Unsteady measurements, for a 20-s time period, of the instantaneous $c_n$ values at the 70% span station of the 8.5-m turbine blade (with a NACA $63_n$-2nn section) show two preferred levels around $c_n \approx 1.45$ and 1.2 (Fig. 2). Measurements on a full-scale wind-turbine blade in a 4 × 4 m open-jet wind tunnel, with the 4-m wide jet centered around the 70% span position, gave the $c_n(\alpha)$ results shown in Fig. 3. At 16 deg < $\alpha$ < 28 deg the double-stall phenomenon is clearly delineated, in spite of the considerable data scatter. Two-dimensional unsteady measurements at $\alpha = 15.3$ deg on a blade section of 1.9 m length, using a scan rate of 100 Hz, gave the results shown in Fig. 4. Three different $c_l$ levels can be identified: $c_l \approx 1.0$, $c_l \approx 1.15$, and $c_l \approx 1.27$. Tuft-flow visualization showed that the three $c_l$ levels were associated with very different flow patterns. The three types of pressure distributions measured for the three $c_l$ levels are displayed in Fig. 5. The suction peak has almost disappeared in the pressure distribution for the low $c_l$ level, whereas the difference between the two other pressure distributions for the intermediate and high $c_l$ levels consists of more subtle changes of the flow separation.

The results are summarized as follows in Ref. 4: "The conclusion for the measurements described above is that $C_L$ can change between three different levels without any measured changes in the external average conditions." Calculations for a NACA 63-215 airfoil section showed the maximum lift to be very sensitive to boundary-layer transition. Three computed pressure distributions for $\alpha = 15$ deg are shown in Fig. 6, i.e., for transition at the leading edge (fully turbulent flow), for free transition fluctuating between 1 and 3% chord; and for

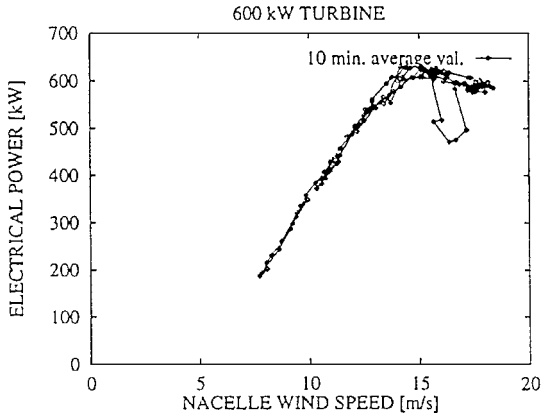


**Fig. 1 Measured 10-min average values of the electrical power for a 600 kW wind turbine.[4]**

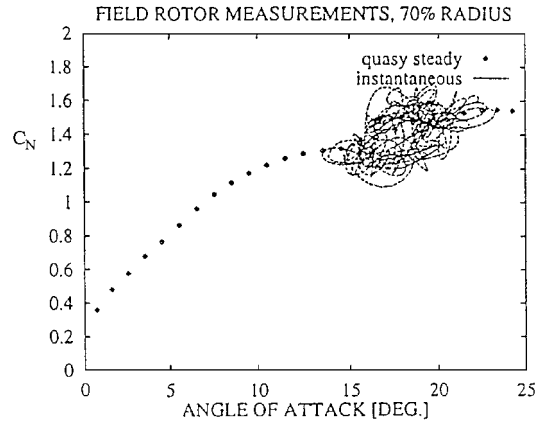


**Fig. 2 Measurement at $Re \approx 1.7 \times 10^6$ of instantaneous $c_n$ at 70% span of a full-scale rotating blade.[4]**

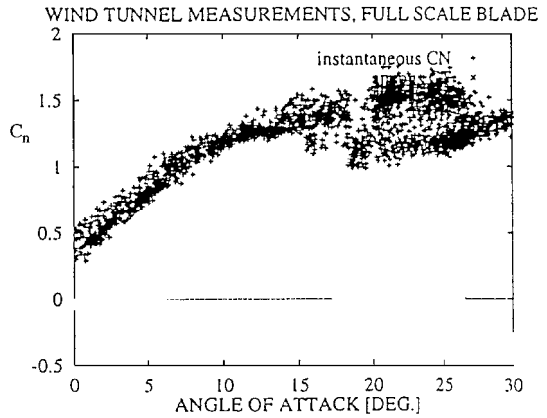


**Fig. 3 Instantaneous wind-tunnel measurements at $\alpha = 15.3$ deg and $Re = 1.3 \times 10^6$ on a section of a full-scale rotor blade in a 4 × 4 m open-jet wind tunnel.[4]**

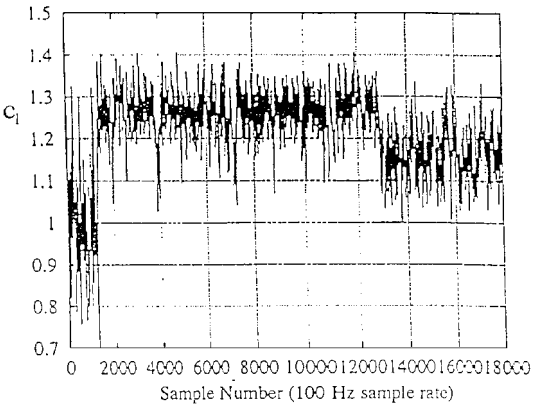


**Fig. 4 Two-dimensional measurements of $c_l = f(t)$ for a total of 180 s on a NACA 63-215 blade section of 1.9-m chord at $\alpha$ = 15.3 deg and $Re = 1.3 \times 10^6$ (Ref. 4).**

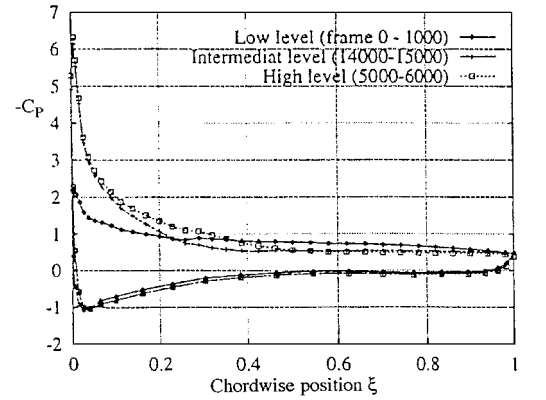


**Fig. 5 Measured time-average pressure distributions for the three distinct $c_l$ levels in Fig. 4 (Ref. 4).**

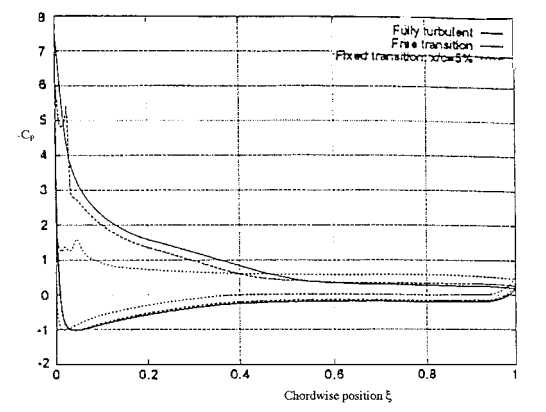


**Fig. 6 Computed pressure distributions for the NACA 63-215 airfoil section for three different flow conditions at $\alpha$ = 15.3 deg and $Re$ = $1.15 \times 10^6$ (Ref. 4).**

fixed transition at 5% chord. Thus, the computations demonstrated that the source of the different lift levels for the NACA 63-215 airfoil section was likely to be the formation of a laminar separation bubble at the leading edge. Based upon the agreement between computations at $\alpha = 15$ deg (Fig. 6) and the measurements at $\alpha = 15.3$ deg (Fig. 5), the conclusion was made that the laminar separation bubble played a decisive role in the double-stall phenomenon occurring in two-dimensional flow. Oil-flow visualization results indicated that the laminar separation bubble also was present near the leading edge of the rotating turbine blade. The observed higher than two-dimensional lift level on the full-scale rotor blade was assumed to be the result of turbulence and three-dimensional flow effects. Stall flutter was recognized as a structural problem: "More seriously, stall induced vibrations seem to be influenced by the quite different flow conditions and corresponding dynamic airfoil forces related to double stall."[4] However, it appeared not to have been considered to play an important role in creating the double-stall phenomenon. The present analysis shows it to be a key flow mechanism in generating the necessary conditions for double stall.

## Analysis

The double-stall phenomenon, as it occurs in two-dimensional flow, is described in Ref. 4, as well as the extension to three-dimensional steady flow. What is needed in addition is an unsteady

flow treatment that can define the flow physics causing the unusual experimental results in Figs. 1–3. Comparing the measured sectional normal-force levels at 70% span on the rotor blade (Figs. 2 and 3) with the sectional lift in the two-dimensional test (Fig. 4), one finds that $c_{l\,\max}$ ($\approx c_{n\,\max}\cos\alpha$) at $\alpha = 15.3$ deg in Figs. 2 and 3 is in agreement with $c_{l\,\max}$ in Fig. 4, indicating that the blade-bending oscillations generated by stall flutter[3] have not yet started at $\alpha = 15.3$ deg. The data scatter for the rotor blade at $\alpha \leq 15.3$ deg in Fig. 3 is in basic agreement with the data scatter for the two-dimensional, stationary airfoil in Fig. 4, being caused in both cases by the general flow unsteadiness of the freestream rather than by the lateral motion of the airfoil section, e.g., in response to stall flutter. However, when the static stall angle is exceeded, $\alpha > 15.3$ deg in Figs. 2 and 3, the sectional lift maximum is increased significantly above the (static) value existing at $\alpha = 15.3$ deg. How this is caused by the stall flutter phenomenon associated with dynamic airfoil stall[5] will be described in what follows.

**Dynamic Airfoil Stall**

When and where flow separation occurs on an airfoil is determined by the boundary-layer profile shape and the adversity of the pressure gradient. The accelerated flow effect on the latter can be determined by applying the unsteady Bernoulli equation. For a pitching airfoil one obtains[5]

$$\frac{dp_e}{dx} = \left(\frac{\partial p_e}{\partial x}\right)_{\alpha=o} + \frac{\partial p_e}{\partial(c\dot{\alpha}/U_e)}\frac{c\dot{\alpha}}{U_e} \tag{1}$$

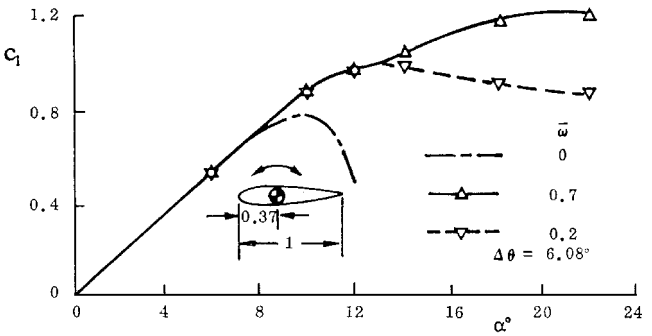


**Fig. 7 Moving-wall-induced leading-edge-jet effect.[7]**

The corresponding dynamic overshoot of static stall can be written as

$$\Delta_1 c_{l\,\max} = c_{l\alpha}\Delta\alpha_{s1} \tag{2a}$$

$$\Delta\alpha_{s1} = K_1(c\dot{\alpha}/U_\infty) \tag{2b}$$

Adding the pitch-rate-induced camber effect and the Karman–Sears wake lag gave satisfactory prediction[3,5] of the experimental results for the VERTOL 23010-1.58 airfoil.[6] The satisfaction with this success lasted until applying the same analytic method to predict the experimental results[7] in Fig. 7. The accelerated flow effect, Eqs. (1) and (2), can only delay the occurrence of flow separation, whereas prediction of the experimental results in Fig. 7 required a flow mechanism that could reattach fully separated flow. At $\alpha_o = 22$ deg the airfoil is in the deep-stall region, and the 6-deg amplitude oscillation can only reach down to $\alpha = 16$ deg, still far above the static-stall angle $\alpha_s \approx 10$ deg. As the data points in Fig. 7 represent the time-average values, it is clear that dynamic lift values more than 100% above static lift maximum must have been generated during the upstroke. A powerful flow mechanism that could produce this is the moving-wall effect[8,9] (Fig. 8). As the wing is pitching or plunging upward during the upstroke, the generated flow velocity $U_W$ at the leading-edge surface has to be equal to the tangential surface velocity of the airfoil in order to satisfy the no-slip condition. When the airflow comes around the corner to the upper surface of the airfoil, the tangential wall velocity has decreased drastically, causing the near-wall boundary layer to be left with an excess velocity. This moving-wall-induced wall-jet effect during the upstroke improves the boundary-layer profile (Fig. 8a), delaying flow separation. On the downstroke the wall-jet effect generates a separation-prone profile, promoting flow separation (Fig. 8b). The effect is crudely illustrated in Fig. 8 by the roller-bearing effect created by a rotating leading-edge cylinder of radius $r_N$.

Experiments[10,11] have shown that wall jets that were too small to be traceable in the measured boundary-layer profiles could eliminate the leading-edge separation bubble. Thus, one could expect that the wall-jet-like moving-wall effect (Fig. 8) may be of sufficient magnitude to cause the large overshoot of static lift maximum required to produce the experimental results in Fig. 7. It has been demonstrated that oscillatory wall jets of miniscule strength can cause reattachment of fully separated flow.[12]

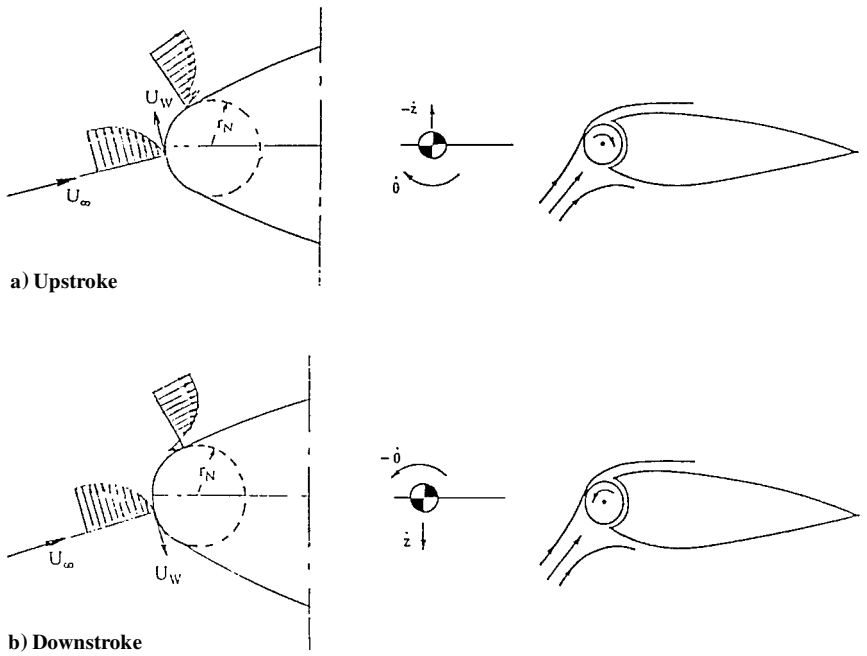


**Fig. 8 Time average $c_l(\alpha)$ curves at $Re = 1.0 \times 10^6$ for thin wing describing 6.08-deg amplitude pitch oscillations of varying frequency.[7]**

Figure 8 shows that the moving-wall effect will influence pitching and plunging airfoils in opposite ways. This explains the failure of the concept of the equivalent angle of attack,[13] Eqs. (3), to account for the difference in dynamic-stall characteristics for pitching and plunging airfoils.

$$\alpha_{\text{eff}} = \alpha_o + \theta^* \tag{3a}$$

$$\theta^* = \bar{\alpha} \sin \omega t \tag{3b}$$

$$\bar{\alpha} = |\theta| = |\dot{z}/U_\infty| \tag{3c}$$

where $\dot{z}/U_\infty$ is the equivalent pitch. The accelerated flow effects, Eqs. (1) and (2), are the same for pitching and plunging airfoils, depending only on the effective angle of attack, Eqs. (3).

The undamping moving-wall effect for the plunging degree of freedom (Fig. 8) generated the negative aerodynamic damping measured by Liiva et al.,[14] for plunging oscillations (of the NACA-0012 and VERTOL 23010-1.58 airfoils) in the alpha region of beginning airfoil stall (Fig. 9). The leading-edge-jet effect (Fig. 8) generates an overshoot of the static-stall angle that in a first approximation can be expressed as[5]

$$\Delta\alpha_{s2} = -K_2(\dot{z}_{\text{LE}}/U_\infty) \tag{4}$$

resulting in

$$\Delta_2 c_{l\,\max} = c_{l\alpha}\Delta\alpha_{s2} \tag{5}$$

The leading-edge-jeteffect, Eq. (4) and Fig. 8, provides the negative damping-in-plunge measured when the mean (time-average) angle of attack exceeds the static-stall angle ($\alpha_o > \alpha_s$ in Fig. 9).

The problem of stall flutter in the pitching or torsional degree of freedom was analyzed as it applied to the straight-wing space shuttle configuration.[5] In the present case stall flutter in the bending degree of freedom is probably of more relevance. For the full-scale rotor blade (Figs. 2 and 3) the torsional stiffnes is likely to be large compared to that for the bending degree of freedom. The moving-wall effect, Eqs. (4) and (5), will drive the bending oscillations as long as the mean angle of attack stays in the initial stall region (corresponding to 10 deg $< \alpha <$ 20 deg in Fig. 9). That would explain the $c_n$ excursions in Figs. 2 and 3. Note that the negative damping-in-plunge implies that $c_n$ increases during the upstroke and decreases during the downstroke. Three-dimensional flow effects and differences in airfoil shapes explain the larger stall angles in Figs. 2 and 3 compared to Fig. 9. The fact that the double-stall phenomenon is much better defined in Fig. 3 than in Fig. 2 is probably a result of the difference in freestream conditions, being constant in Fig. 3 but varying in Fig. 2 with the blade position in the Earth boundary layer as a function of blade rotation.

The experimental results for the (nominally) stationary rotor blade in Fig. 3 show, as expected, that the plunging-induced moving-wall effect[15] is more effective in promoting flow separation during the downstroke than in delaying separation during the upstroke (Fig. 8),

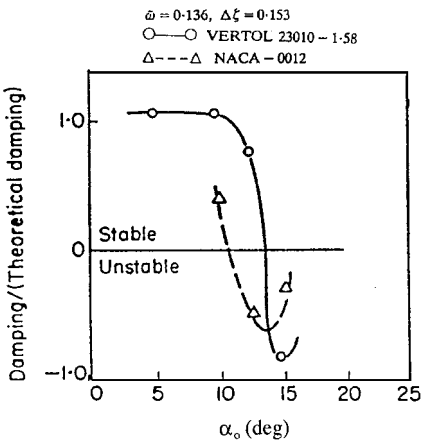


**Fig. 9 Stall-induced loss of damping of airfoils oscillating in plunge.[14]**

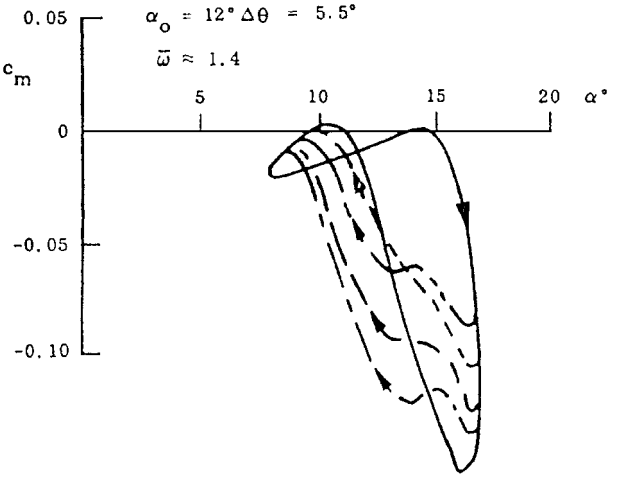


**Fig. 10 Nonrepeating backstroke portion of consecutive $c_m(\alpha)$ loops of the Vertol 23010-1.58 airfoil in the dynamic-stall region.[18]**

producing a low $c_n$ level that is below the prestall value and a high $c_n$ level that is only slightly above it. The results in Fig. 2 for the rotating rotor blade are different, with the upstroke motion having a stronger effect than the downstroke motion, producing the eye-catching result that the time-average (quasi-steady) deep stall $c_n(\alpha)$ deviates upward from the prestall data trend, with the mean $c_n$ values approaching the maximum instantaneous measurements. The rotation-induced span-wise flow component could possibly explain some of the difference between the instantaneous $c_n$ for a stationary (Fig. 3) and a rotating blade (Fig. 2). However, that would not explain the fact that the time-average $c_n$ lies close to the maximum, instantaneous $c_n$ values. This requires its own explanation.

In the case of leading-edge stall, as for the NACA-0012 airfoil, the travel down the chord of the spilled leading-edge vortex[16,17] is generating lift after that stall has occurred. During the backstroke part of the oscillation, this spilled vortex continues to generate lift if $\bar{\omega} > 1$, so that vortex-induced lift is still present during part of the backstroke. This could be responsible for the observed high time averaged $c_n$ in Fig. 2. The same spilled vortex phenomenon was probably responsible for the nonrepeating nature of the backstroke $c_m$ loops for the Vertol 23010-1.58 airfoil, pitching at $\bar{\omega} = 1.4 > 1$ (Ref. 18 and Fig. 10). In the absence of stall flutter, there would be no moving-wall effects that could increase the lift in the deep-stall alpha region to exceed the prestall lift maximum.

### Transition in Unsteady Flow

An examination of the double-stall phenomenon (Fig. 1) requires a study of how the moving-wall effect influences boundary-layer transition.[19] The influence of the moving wall effect on flow separation changes dramatically when it occurs via its action on transition. The Magnus lift results for a rotating circular cylinder[20] (Fig. 11) are instructive. In the case of laminar, incipient flow separation, the Magnus lift is generated mainly by the power of the downstream moving-wall effect to delay separation on the top side, shifting separation from the subcritical toward the supercritical position. On the bottom side the separation is already of the subcritical type, and there is little room for the moving-wall effect to promote separation. In the case of turbulent, initial flow separation, the situation is reversed. The main influence is the upstream moving-wall effect on the bottom side, promoting separation, moving it from the supercritical toward the subcritical position. On the top side the separation is already supercritical, and the downstream moving-wall effect has limited possibility of delaying the separation further. In both cases positive Magnus lift is generated.

The moving-wall effects on laminar and turbulent flow separations are rather straightforward and explain the positive Magnus-lift-slope $\partial c_l/\partial(U_W/U_\infty) > 0$ in Fig. 11. The negative slope, the so-called Magnus-lift-reversal, is caused by the moving-wall effect on transition. At critical flow conditions (curves $j$ and $k$ in Fig. 11) the downstream moving wall effect on the top side delays transition

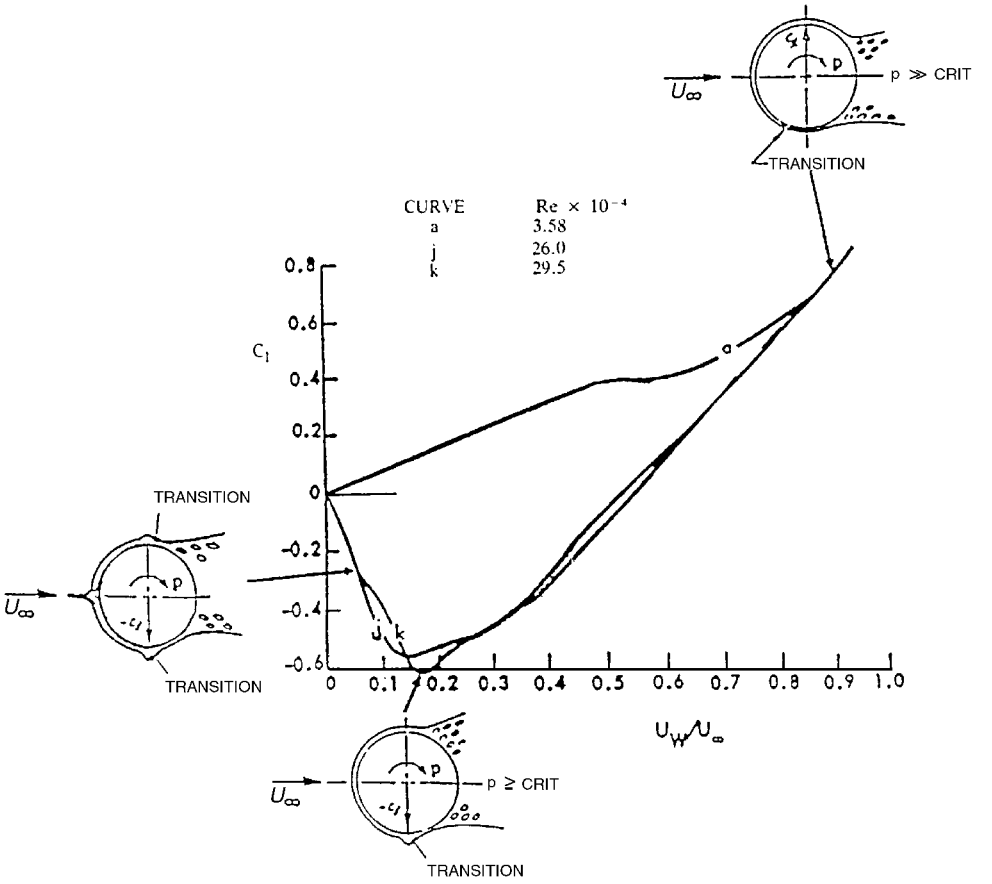


**Fig. 11 Magnus lift on a rotating circular cylinder at critical flow conditions.[20]**

in the laminar separation bubble, causing a loss of lift. On the bottom side the upstream moving-wall effect promotes transition in the bubble, producing increased suction, thereby also generating a negative lift component. Thus, both top and bottom sides contribute to the measured negative Magnus-lift-slope $\partial c_l / \partial (U_W / U_\infty) < 0$ for $U_W / U_\infty < 0.1$ in Fig. 11. This explains why the lift loss is twice as large at critical flow conditions as for initially laminar or turbulent flow separation.[15] In the case of flat spin,[21] a damping yawing moment is measured at rotation rates where the critical flow conditions at $U_W / U_\infty < 0.1$ in Fig. 11 are established[22] ($\Omega < 0.5$ in Fig. 12). Likewise, the negative lift generated at critical flow conditions will produce damping for plunging oscillations of the circular cylinder. Accordingly, the moving-wall effect on the laminar separation bubble on the top of an airfoil will at critical flow conditions generate damping for plunging oscillations.

Because "The critical Reynolds and the operating Reynolds number are of the same order of magnitude" ($1.2 \times 10^6 < Re < 2.3 \times 10^6$) (Ref. 4), one can assume that the power bucket in Fig. 1 is generated at critical flow conditions. Thus, one can construct the following scenario: A sudden large-amplitude downstroke excursion of the plunging oscillations, caused by a wind gust, for example, could produce the large moving-wall effect needed to promote transition to occur upstream of the laminar separation bubble, thereby eliminating it. This would result in the turbulent low-lift pressure profile shown in Figs. 5 and 6, generating the low-lift level of the double-stall phenomenon, with associated low power level (Fig. 1). When the gust has passed and the associated turbulent flow conditions have disappeared, the critical flow conditions generating the laminar separation bubble are reestablished. However, as was discussed earlier for the range $U_W / U_\infty < 0.1$ in Fig. 11, the moving-wall effect will have a damping effect on the plunging oscillations.[9] As a consequence, the low-lift level and associated low power level (Fig. 1) will persist as long as the wind speed remains in the critical flow region. If $U_\infty$ is changed such that laminar or turbulent

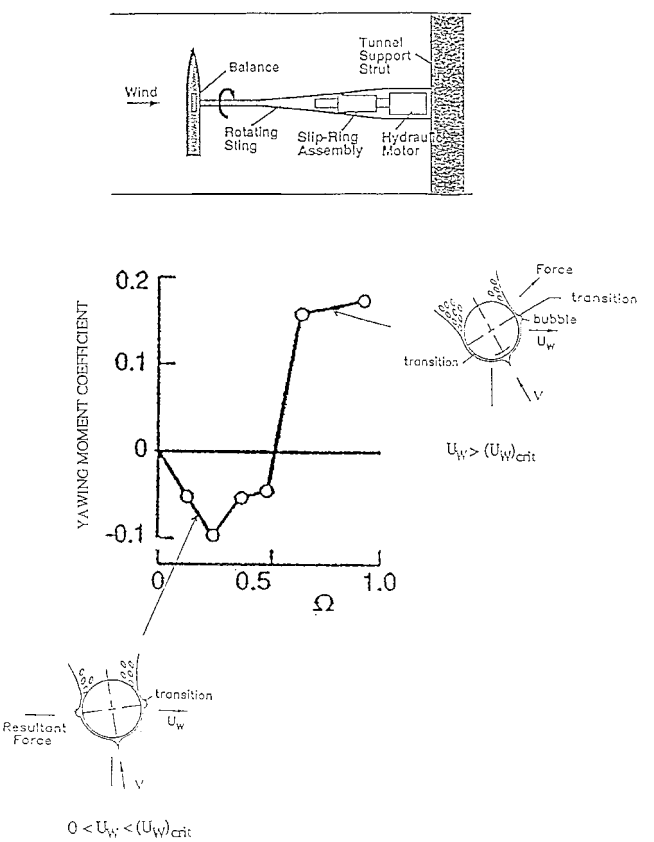


**Fig. 12 Yawing moment measured on cone cylinder driven in flat spin.[22]**

flow separation occurs on the turbine blade, the moving-wall effect becomes undamping[9] (Figs. 8 and 9), and the blade section will describe plunging oscillations with increasing amplitude, generating high-lift levels. According to this scenario, a transfer from the low- to the high-lift level could only occur outside of the critical flow region, defined as 15 m/s < $U_\infty$ < 17 m/s by the results in Fig. 1.

## Conclusions

Based upon an analysis of experimental and computational results for the stalled flow that occurs on the rotor blades of wind turbines operating at full power, the necessary conditions for the observed double-stall phenomenon to be generated are as follows:

1) The airfoil shape is such that at the Reynolds numbers of interest a laminar separation bubble can be formed near the leading edge.

2) At steady-state freestream flow conditions two different high-lift levels can be established in the (early) deep-stall region depending upon where boundary-layer transition occurs on the airfoil section.

3) At the unsteady separated flow conditions existing on the blade of a wind turbine operating at full power, the blade's bending response to stall flutter produces moving wall effects on the plunging blade sections. At wind velocities generating critical crossflow conditions for the blade sections, these moving-wall effects control where boundary-layer transition occurs, thereby determining whether or not the double-stall phenomenon will occur.

4) Outside the critical crossflow region the moving-wall effects generated by stall flutter cause the deep-stall time-average lift of the blade section to exceed the static lift maximum.

## Acknowledgment

This paper benefited from the insightful comments made by the reviewers.

## References

[1]Rasmussen, F., Petersen, J. T., and Madsen, H. A., "Dynamic Stall and Aerodynamic Damping," AIAA Paper 98-0024, Jan. 1998.

[2]Ericsson, L. E., and Reding, J. P., "Fluid Mechanics of Dynamic Stall, Part I, Unsteady Flow Concepts," *Journal of Fluids and Structures*, Vol. 2, Jan. 1988, pp. 1–33.

[3]Ericsson, L. E., and Reding, J. P., "Stall Flutter Analysis," *Journal of Aircraft*, Vol. 10, No. 1, 1973, pp. 5–13.

[4]Madsen, H. A., Bak, C., Fuglsang, P., and Rasmussen, F., "The Phenomenon of Double Stall," EWEC 97, Paper 1997.

[5]Ericsson, L. E., and Reding, J. P., "Unsteady Airfoil Stall, Review and Extension," *Journal of Aircraft*, Vol. 8, No. 8, 1971, pp. 609–616.

[6]Liiva, J., "Unsteady Aerodynamics and Stall Effects on Helicopter Rotor Blade Airfoil Sections," *Journal of Aircraft*, Vol. 6, No. 1, 1969, pp. 46–51.

[7]Halfman, R. L., Johnson, H. C., and Haley, S. M., "Evaluation of High-Angle-of-Attack Aerodynamic-Derivative Data and Stall-Flutter Prediction Techniques," NACA TN 2533, 1951.

[8]Ericsson, L. E., and Reding, J. P., "Analytic Prediction of Dynamic Stall Characteristics," AIAA Paper 72-682, June 1972.

[9]Ericsson, L. E., "Moving Wall Effect in Relation to Other Dynamic Stall Flow Mechanisms," *Journal of Aircraft*, Vol. 31, No. 6, 1994, pp. 1303–1309.

[10]Wallis, R. A., "Boundary Layer Transition at the Leading Edge of Thin Wings and Its Effect on General Nose Separation," Advances in Aeronautical Sciences, American Astronautical Society, San Diego, CA, 1970, pp. 161–184.

[11]Wallis, R. A., "The Turbulent Boundary Layer on the Articulated Nose of a Thin Wing Provided with Air Jets," Aeronautical Research Lab., Aero Note 141, Australia, Oct. 1954.

[12]Wygninski, I., and Seifert, A., "The Control of Separation by Periodic Oscillations," AIAA Paper 94-2608, June 1994.

[13]Carta, F. O., "A Comparison of the Pitching and Plunging Response of an Oscillating Airfoil," NASA CR 3172, Oct. 1979.

[14]Liiva, J., Davenport, F. J., Gray, L., and Walton, I. C., "Two-Dimensional Tests of Airfoil Oscillating Near Stall," U.S. Army Aviation Lab., TR 68-13, Fort Eustis, VA, April 1968.

[15]Ericsson, L. E., "Moving Wall Effects in Unsteady Flow," *Journal of Aircraft*, Vol. 25, No. 11, 1988, pp. 979–990.

[16]Ericsson, L. E., and Reding, J. P., "Dynamic Stall of Helicopter Blades," *Journal of the American Helicopter Society*, Vol. 17, No. 2, 1972, pp. 11–19.

[17]Ham, N., and Garelick, M. S., "Dynamic Stall Considerations in Helicopter Rotors," *Journal of the American Helicopter Society*, Vol. 13, No. 2, 1968, pp. 44–55.

[18]Liiva, J., and Davenport, F. J., "Dynamic Stall of Airfoil Sections for High Speed Rotors," Paper 206, *24th Annual National VISTOC Forum of the American Helicopter Society*, May 1968.

[19]Ericsson, L. E., "Effects of Transition on Wind Tunnel Simulation of Vechicle Dynamics," *Progress in Aerospace Sciences*, Vol. 27, 1990, pp. 121–144.

[20]Swanson, W. M., "The Magnus Effect: A Summary of Investigations to Date," *Journal of Basic Engineering*, Vol. 83, Sept. 1961, pp. 461–470.

[21]Ericsson, L. E., and Beyers, M. E., "Flat Spin of Axisymmetric Bodies," *Journal of Aircraft*, Vol. 32, No. 6, 1995, pp. 1205–1212.

[22]Ericsson, L. E., and Beyers, M. E., "Viscous-Flow/Vehicle-Motion Coupling of Rotary Flows, Rotary Balance Testing for Aircraft Dynamics," AGARD-AR-265, Dec. 1990, Chap. 8, pp. 164–167, 183–187.